Article:

Lu, Y., Tang, J., Xu, X. et al. (2 more authors) (2024) Characteristics of Warm-Season Mesoscale Convective Systems Over the Yangtze–Huaihe River Basin (YHR): Comparison Between Radar and Satellite. Journal of Geophysical Research: Atmospheres, 129 (1). e2023JD038924. ISSN 2169-897X

https://doi.org/10.1029/2023jd038924

Characteristics of Warm-season Mesoscale Convective Systems over the Yangtze-Huaihe River Basin (YHR)—comparison between radar and satellite

Yutong Lu[1,2,3], Jianping Tang[1,2], Xin Xu[1,2], Ying Tang[4], Juan Fang[*,1,2]

[1] Key Laboratory of Mesoscale Severe Weather/Ministry of Education, Nanjing University, Nanjing, 210023, China.

[2] School of Atmospheric Sciences, Nanjing University, Nanjing, 210023, China.

[3] Institute for Climate and Atmospheric Science, School of Earth and Environment, University of Leeds, Leeds, LS2 9JT, United Kindom.

[4] Nanjing Marine Radar Institute, Nanjing, 211153, China.

Corresponding author: Juan Fang (fangjuan@nju.edu.cn)

To be submitted to JGR-A

Key points

1. Six-year climatology of warm-season MCSs in YHR are investigated using satellite, radar data and ERA5.

2. Criteria setting for tracking MCSs significantly influences the derived features.

3. Meiyu season MCSs featured longest duration, largest areas and heaviest precipitation, while the background circulation anomalies are the weakest.

Abstract

Mesoscale convective systems (MCSs) are crucial in modifying the water cycle and frequently induce high-impact weather events over eastern China. Radar and CPC-4km satellite-derived infrared cloud top temperature (Tb) data were used to thoroughly analyze the long-term climatology of MCSs over eastern China, particularly in the Yangtze-Huaihe River Basin (YHR) in the warm season from 2013 to 2018. For the first time, we contrasted the effects of dataset selection and threshold setting on research outcomes. The large-scale environments of MCSs initiation were also investigated using the latest global reanalysis data ERA5. It is found that striction of thresholds, including duration, reflectivity/Tb, area, and linearity, would lead to a greater proportion of early-morning MCSs. Satellite-identified MCSs differed from radar-derived ones, exhibiting afternoon diurnal peaks, faster movement speeds, longer travel distances, and expansive impact areas. The centre of MCS and related precipitation shifted northward from Pre-meiyu to Post-Meiyu seasons, contributing to up to 20% of total rainfall, with most MCSs moving along eastward trajectories. MCSs typically had the most significant impact in the Meiyu season because of the most prolonged duration, largest convective core area, and strongest precipitation intensity. Warm season MCSs initiated ahead of mid-level troughs and were related to strong anomalous low-level convergence and mid-level upward. The circulation anomalies were the strongest in the Pre-Meiyu season among the three sub-seasons, with most moisture sourced from the southwest.

Plain Language Summary

This work used radar and satellite data to analyze the climate characteristics of a kind of large thunderstorms known as mesoscale convective systems (MCS) in the Yangtze-Huaihe River Basin (YHR) in eastern China. These systems cover large areas, lasting from a few hours to a few days. The analysis revealed that stricter tracking thresholds would lead to more early-morning MCSs. Satellite-identified MCSs differed from those identified by radar. They tended to have more thunderstorms in the afternoon, move faster, travel longer distances, and cover larger areas. MCSs also contributed to up to

20% of the total warm-season rainfall in the YHR. MCSs typically had the most significant impact in the rainy season of eastern China from mid-June to mid-July. Warm season MCSs initiated ahead of low-pressure systems and were related to strong anomalous low-level convergence and mid-level upward motion. During the time before the rainy season, the large-scale forcing needed to be anomaly enough to trigger MCS formation. Most of the moisture that caused MCSs came from southwest direction instead of stemming locally during this period.

1. Introduction

Mesoscale convective systems (MCSs) are organized clusters of deep convective clouds with contiguous areas of precipitation larger than 100km at least in one direction and last several hours (Houze, 2004). MCSs contribute a large portion of total precipitation over areas including North America and China (Feng et al., 2018, 2019; Jirak & Cotton, 2007; Kukulies et al., 2021; Li et al., 2020) and have drawn much attention for causing high-impact extreme weather events, especially floods (Moore et al. 2012; Hu et al. 2021; Atiah et al. 2023). Flooding can often result from MCS rainfall with considerable size, long duration, and slow movement (Haberlie & Ashley, 2019; Nesbitt et al., 2006). For instance, several flood events in eastern China (Wang et al. 2015; Yin et al. 2022; Wei et al. 2023) are indicated to be related to one or multiple MCSs. Under global warming, climate projections suggest that the frequency and intensity of MCS have increased (Feng et al. 2016; Taylor et al. 2017; Hu et al. 2020) and are expected to enhance in the future, casting higher demand for understanding climatology characteristics and related weather hazards.

The climatology of MCSs, both globally and in specific regions such as the tropics, North America, and eastern China, has been extensively studied (Barnes and Houze, 2015; Pfister et al. 1993; Anselmo et al. 2021; Haberlie and Asheley, 2019; Cui et al. 2021). In eastern China, MCSs occur in three latitudinal zones, 20°, 30°, and 50°N, with frequency decreasing from lower to higher latitudes (Yang et al. 2015; Li et al. 2020). In addition to spatial distribution, MCSs have significant temporal variability, affecting the interannual, seasonal, sub-seasonal, and hourly scale variability of precipitation in the region (Yang et al. 2015; Li et al. 2020).

The Yangtze-Huaihe River basin (YHR) is one of the most developed regions in eastern China. Under the control of the Asian summer Monsoon, YHR is influenced intensively by active Meiyu fronts during the warm season, which creates a favourable environment with abundant moisture and active uplifting to initiate MCSs and thus brings about heavy precipitation. Previous research indicated that the YHR exhibits the most pronounced seasonal cycle of MCS precipitation in eastern China, over 2.6mm/day in June (Li et al. 2020), contributing to around 30% of the total precipitation in the warm season (Yun et al. 2021). Therefore, understanding the characteristics of MCSs over YHR is substantial for disaster prediction and prevention.

However, the climatic characteristics and properties (e.g., area, propagation speed, track length, precipitation intensity) of MCSs generated each year in eastern China differ between studies.

The ability of different types of datasets to characterize MCS varies. For example, the frequency of MCSs south of the Yangtze River in the warm season obtained by Li et al. (2020) using precipitation observations is quite different from those obtained by Yang et al. (2015) using FY-2 satellite-derived infrared cloud top temperature over the similar region. The features of MCSs can also be different, while certain metrics can be similar between studies. For example, the MCS precipitation contribution to the total precipitation in the Yangtze-Huaihe River basin calculated by Kukulies et al. (2021) was around 25% which is close to the 30% result derived by Li et al. (2020). Previous studies have made progress in tracking and analyzing the climatology of MCSs over eastern China using satellites (Yang et al. 2015; Chen et al. 2019; Li et al. 2020), radar observations (Zheng et al. 2013; Tang et al. 2020) and precipitation data (Li et al. 2020; Yun et al. 2021). Infrared (IR) data of cloud top temperature from geostationary satellite data are often used to identify MCS by determining from continuous satellite imagery whether cloud top temperatures meet the established thresholds. However, the cold cloud region is not entirely equivalent to the intense precipitation region, leading to errors in the detection of MCSs (Feng et al. 2021). On the contrary, radar reflectivity data can reveal the convective structure beneath cold clouds and reflect the distribution of convective and stratiform clouds in mature MCSs, playing an essential role in studying the formation mechanism of MCSs (Houze et al. 1989; Cetrone and Houze, 2009; Wang et al. 2019). However, in long-term climate studies, radar data is restricted by spatial and temporal heterogeneity and limited observational range over eastern China.

Moreover, the discrepancies in MCS definitions can also lead to controversial results on MCS climatology. Previous studies using the data mentioned above usually identified MCSs by automatic object-based tracking algorithms using a set of criteria and thresholds. However, there is no common standard on intensity, time persistence, spatial extent, shape, etc. With radar reflectivity data, for example, Tang et al. (2020) defined MCSs in the YHR as convective areas with reflectivity over 35dBZ $\geq$1000km^2 with at least one direction longer than 100km and lasting more than 3 hours. Using cloud-top brightness temperature (Tb) data, Jirak et al. (2003) picked out MCSs from the Mesoscale Convective Complexes (MCCs) defined by Maddox (1980) based on the findings by Bartels et al. (1984) and further developed the definition into four MCS categories, and the most lenient condition is: 1) cold cloud region $\leq$-52°C with area $\geq$30000km^2, 2) lasting longer than 3 hours, 3) eccentricity $\geq$0.2 at time of maximum extent. The classification and criteria are further modified and adopted in several studies focusing on eastern China (Yang et al. 2015; Liu et al. 2021). These differences can lead to biases in the influence of MCSs and induced weather events under long-term climate (Kukulies et al. 2023). Therefore, looking into any potential effects the threshold settings may have on the MCSs' properties is essential.

Motivated by the above reasons, in this study, we aim to investigate the climatological characteristics of MCSs and MCS-induced precipitation over YHR for six years (2013–2018) from April to September with multi-year Doppler radar observations, NOAA (National Oceanic and Atmospheric Administration) CPC (Climate Prediction Center) Satellite data and IMERG precipitation data, and discuss the influence of dataset and definition of MCSs. The remainder of this paper is organized as follows. Section 2 describes the identification methods, evaluation metrics, and observational and reanalysis datasets used in this study. In Section 3, the results of sensitivity tests of MCS definition, MCS climatological features, and related precipitation characteristics are shown and discussed. Section 4 demonstrates the large-scale background circulation during the initiations stage of MCS in warm seasons. The main conclusions are summarised in Section 5.

2. Data and Methods

2.1 Observational and reanalysis datasets

MCSs in the YHR were identified and tracked using CPC-4km, satellite-derived IR brightness temperature (Tb) data with a horizontal resolution of 4 km released by the CPC (Janowiak et al. 2001). The CPC-4km dataset, merging different infrared channels of geostationary meteorological satellites currently in operation (visible channels are not included), can provide a global (60°S–60°N) coverage every 30 minutes and has undergone viewing angle and parallax corrections. Previous studies have utterly utilized the CPC-4km Tb data to track MCSs by identifying cold clouds related to deep convections (Salio et al. 2007; Rehbein et al. 2018; Hu et al. 2021; Cheng et al. 2022). The merged precipitation data (IMERG), a multi-satellite derived precipitation retrieval product launched in the Global Precipitation Measurement (GPM) mission by NASA with a spatial resolution of 0.1 degree and a temporal resolution of 30 minutes, was integrated into the MCS tracking algorithm. Since IMERG might offer the "best" precipitation estimations, IMERG has drawn attention and is employed in many fields (Ayat et al. 2021; Bolvin et al. 2021; Jiang et al. 2019) and is evaluated or used for studying MCS precipitation (Hayden et al. 2021; Kukulies et al. 2021; Feng et al. 2021; Chen et al. 2022).

The analysis of MCSs over YHR also uses Doppler radar observations from April to July. The raw radar data were pre-processed and bilinearly interpolated into a 4km grid using the 88D2ARPS program of the Advanced Regional Prediction System (APRS, Xue et al. 2000) following Tang et al. (2020). Data quality control was first conducted, including removing non-meteorological echoes and de-aliasing radial velocity (Brewster et al. 2005). The radar observation covers the area of 110°E–125°E, 27°N–40°N from seventeen stations, namely Nanhui (9210), Nanjing (9250), Wuhan

(9270), Zhengzhou (9371), Nantong (9513), Yancheng (9515), Xuzhou (9516), Huaian (9517), Lianyungang (9518), Changzhou (9519), Taizhou (9523), Jinan (9531), Qingdao (9532), Hefei (9551), Fuyang (9558), Tongling (9562) and Hangzhou (9551), each of them detects an area with a diameter of 230km (Fig. 1A). The maximum value at each pixel within radar overlap regions was selected, which is a common approach in radar mosaic processing.

Considering the detection range and inhomogeneity of radar detection, we chose 110°E–125°E, 27°N–40°N as the MCS detection area, and 114°E–122°E, 30°N–36°N as the analyzing area, where radar sites are sufficient and dense. Only MCSs initiating in the analyzing area were counted in the evaluation.

2.2 MCS Tracking

The MCS thresholds to be tested are listed in Table 1, and S_P Def 1 was selected after sensitivity tests (described in Section 3.1). To identify and track MCSs over YHR, an objected-based tracking (OT) algorithm was developed. The OT algorithm can be exploited to track various systems with diverse datasets by altering thresholds and selecting process procedures. The study of Guo et al. (2022), which employed the OT algorithm to look into the features of precipitation systems and extreme precipitation across eastern China, demonstrated the viability of the OT method. In this work, the algorithm was modified to account for radar reflectivity and CPC-4km TB data, and a process to calculate the precipitation feature (PF) of potential MCS was included.

2.2.1 Convection identification and tracking

For consistency, radar reflectivity data was first interpolated into the same grid as CPC-4km Tb data, and only data at 00 and 30 minutes of each hour were used. The two datasets were then upscaled to an 8km horizontal resolution by taking a simple average of values at all grid points within an 8km radius of each grid point (Clark et al. 2014). The "smoothing" procedure can reduce over-segmentation and filter out small-scale signals to better identify mesoscale systems. To match with the upscaled Tb data, IMERG was interpolated into the 8km grid as well.

The identification and tracking method takes five steps. First, the regions that satisfied the value and area thresholds at each time step were marked as convective core during the identification stage. Second, each convective core was expanded outward pixel by pixel to recognize the surrounding continuous areas with warmer cloud top temperature (or lower radar reflectivity), and the expanded area was considered as the potential stratiform cloud. The entire region was referred to as a cold cloud. If two or more convective cores existed at the same time, the largest core was prioritized for expansion, followed by the smaller ones. The expansion stopped when two adjacent cold clouds encountered each other at their boundaries. Third, the precipitation areas within each cold cloud are identified as a PF, and the relevant characteristics (precipitation rate, long axis, and LWR) are extracted. Fourth, the area overlapping method was adopted in the OT algorithm to connect cold clouds across successive time steps. Two cold clouds would be regarded as belonging to the same potential MCS if they overlapped for more than 50% of space in two successive time steps. If more than two cold clouds overlapped, the larger was included, while the smaller was assumed to end. If a cold cloud split, we assigned the largest split cloud to the potential MCS and initialized the smaller one as a new potential MCS at this time step. Tracking was performed on successive half-hourly data sets until the cold cloud area no longer met the 50% overlapping area criteria. Finally, all potential MCSs' durations and the PF's durations were examined to identify those exceeding the time criteria. The Tb-PF combined method has been used in recent research by Feng et al. (2021) and Kukulies et al. (2021). The potential MCSs passed the duration selection (and PF examination for tracking using satellite data) were labeled as MCS_1, MCS_2, …, MCS_N, where N stands for the number of MCSs we have traced.

2.2.2 Example of an MCS case

Figs. 1a–l depicts the influenced areas of six randomly selected MCS examples detected by our tracker using radar and satellite data on 4th July 2013 (Case 1, Figs. 1a, b), 1st June 2014 (Case 2, Figs. 1e, f), 2nd June 2015 (Case 3, Figs. 1i, j), 2nd August 2016 (Case 4, Figs. 1c, d), 10th June 2017 (Case 5, Figs. 1g, h), and 18th August 2018 (Case 6, Figs. 1k, l), respectively. The affected areas of MCSs observed via radar and satellite are generally identical, although the MCSs generated from satellite tend to affect broader areas except for Cases 1 and 2. Figs. 1a–l also display the traveling routes of the MCSs to give examples of the centroid of objects and their trajectories that the OT algorithm catches. The trajectories of radar- and satellite-based MCSs are typically identical, notably for Case 2. In Case 4–6, the satellite-derived track lengths are significantly longer than those obtained from radar, which may be attributed to either an earlier beginning or a later dissipation. This phenomenon is because IR temperatures not only reflect deep clouds and convections but also high-altitude or cold clouds unrelated to convective in nature. The discrepancy in the observational aspect of MCS by radar and satellite may lead to such controversy in the conclusions. These results indicate that the MCSs monitored by the OT algorithm utilizing both radar and satellite data are generally consistent. In the following research, the OT algorithm serves as a foundation for understanding the features of MCSs.

3. Characteristics of MCSs over YHR

3.1 Effects of tracking criteria on MCS features

To fully comprehend how the choice of MCS thresholds affects the outcomes of MCS climatology, we tested our tracking with different thresholds of MCSs (as listed in Table 1). Five kinds using radar reflectivity data and five kinds using CPC-4km Tb data merging with IMERG precipitation data were first examined to inspect how the factors, including thresholds of linearity, area, duration, and intensity of PF, can affect MCS properties. The key features of tracked MCSs identified by five different tracking criteria using Radar and Satellite data are illustrated in Figure 2.

Firstly, MCSs obtained from radar data under five different criteria are assessed in this part. The influence of the extent of linear shape can be revealed by comparing R_Def 1 and 2. The frequency of MCS is affected by the linearity constraint, declining as the LWR threshold increases (Fig. 2a). However, the seasonal cycle peaks of MCSs vary between R_Def 1 and R_Def 2. Def 1 peaks in July, while R_Def 2 peaks in June, suggesting that the most linear MCSs tend to occur in June, and a strict LWR setting may filter out MCSs with a near-round shape (Fig. 2a). Comparing R_Def 1 and R_Def

3 shows that the duration threshold also affects MCS frequency. With the duration threshold set to 4 hours, R_Def 3 detected approximately half of the MCSs detected by R_Def 1. Additionally, increasing the reflectivity threshold leads to a significant decrease in MCS frequency. This can be observed from the annual cycle of R_Def 4 that in most months, the MCS frequency of R_Def 4 is approximately one-third that of R_Def 1 (Fig. 2a). Area threshold also impacts MCS frequency. Expanding the area threshold to twice that of Def 1 reduces MCS counts, such as in April (R_Def 5).

The diurnal cycles of MCSs with different criteria are illustrated in Fig2. 1b. MCSs with lenient LWR limitation tend to have dual peaks at midnight (2100–0300 LST) and in the afternoon (1500–1800 LST). The bimodal diurnal cycle is particularly significant for Def 1 (Fig. 2b). However, the afternoon peak vanishes as the LWR was increased to ≥4 (R_Def 2, Fig. 2b), suggesting that linear MCSs require time to develop and concentrate, whereas MCSs with rounded convection cores tend to form in the late afternoon. Moreover, a stricter area threshold leads to a more pronounced midnight peak in the diurnal cycle compared to R_Def 1, while the afternoon peak weakens.

The peak of the probability density function (PDF) of propagation speed (Fig. 2e) shifts toward higher values as the LWR threshold increases. R_Def 2, peaking at 60–90 km/h with around 35%, exhibiting more fast-moving MCSs (≥60 km/h) and fewer at lower speeds (≤60 km/h). Comparing R_Def 4 and R_Def 1, a stronger reflectivity threshold shifts the MCS speed PDF peak to higher speeds. R_Def 4 peaks at 60–90 km/h, approaching 50%, with a greater proportion of MCSs exceeding 90 km/h than R_Def 1. Similarly, R_Def 3 shows that stricter time thresholds maintain a consistent peak of speed PDF with R_Def 1, at about 58% in the 30–60 km/h range, slightly lower by 2%. However, there is a higher proportion of fast-moving MCSs (60–90 km/h) in R_Def 3, accounting for approximately 26%, while fewer slow-moving MCSs (0–30 km/h) at approximately 11% compared to R_Def 1. On the contrary, a stronger area threshold (R_Def 5) increases the proportion of slow-moving MCSs (0–30 km/h) compared to R_Def 1, at approximately 25%, while reducing the proportion of fast-moving MCSs (60–90 km/h) to around 10%.

For track length (Fig. 2d), linear MCSs (R_Def 2) moving farther than rounder

MCSs (R_Def 1), with a reduced proportion within 0–400 km (around 76%) and a larger proportion surpassing 400 km compared to R_Def 1. Comparing R_Def 1 and R_Def 4, intensified reflectivity threshold does not necessarily result in longer MCS propagation. Despite the higher percentage of high-velocity MCSs in R_Def 4, this result may stem from the increased presence of short-lived MCSs (Fig. 2c), with the peak in the 3–7 h range, above 80%. A similar trend arises in the comparison between R_Def 5 and R_Def 1 when the area threshold intensifies. The proportion of shorter travel distances rises, with approximately 82% of MCSs falling within 0–400 km. This primarily results from an increased proportion of slower-moving MCSs. The track length proves responsive to duration constraints, with MCSs traveling farther (comparing R_Def 1 and R_Def 3, Figs. 2e, d).

The PDF of the MCS coverage area shown in Fig. 2f is notably impacted by the LWR threshold. Compared to Def 1, the PDF of Def 2 exhibits two peaks. A substantial peak of roughly 7% is evident within 1,000–20,000 km^2, and a generally higher proportion of MCSs areas exceeding 60,000 km^2, suggesting broader influence potential. The area is also sensitive to convective intensity, as seen from the comparison between R_Def 4 and R_Def 1. The convection core area PDF peak in R_Def 4 shifts towards smaller areas as the reflectivity threshold strengthens, reaching its highest point within 1,000–20,000 km^2, accounting for around 85% of the total. A strengthened duration threshold can bring in a smaller proportion of small-area MCSs and a larger proportion of large-area MCSs, as R_Def 3 has a smaller share of MCSs within 1,000–20,000km^2 and a more prominent peak of PDF of around 40% within 20,000–40,000 km^2, compared to R_Def 1. And R_Def 3 features a larger proportion of MCSs exceeding 60,000 km^2.

Furthermore, features of MCSs derived from five definitions using satellite data merging with IMERG precipitation are presented. In S_Def 1, only the cloud-top brightness temperature is used, while S_Def 2–5 incorporate limitations based on PFs. The comparison between S_Def 2 and S_Def 1 shows that the characteristics of MCSs in the YHR are not sensitive to the limitation of PF (when the precipitation rate is set to ≥2mm/h). The comparative analysis of the annual cycle, diurnal cycle, duration, track length, speed, and convective core area of MCS does not show significant differences (Figs. 2g–l). If the duration threshold is stricter, extending from 3 hours (S_Def 2) to 6 hours (S_Def 3), the MCS counts can reduce dramatically, particularly in JJA, indicating that in spring and autumn, long-lived MCSs make up a larger proportion (Fig. 2g). Shorter-lived convective clouds are more common in the summer, meaning that a stricter constraint on duration filters out more systems during summer compared to spring and autumn. Moreover, the diurnal cycle of MCS derived by S_Def 3 shows a unimodal cycle similar to previous definitions, but a greater portion of midnight MCSs are generated (Fig. 2h). As can be seen from the comparison of S_Def 2 and S_Def 4, the counts of MCS increase dramatically, especially in spring, by three times when the temperature threshold value gets higher (Fig. 2g). The diurnal cycle also shows that more MCSs generate in the afternoon and fewer MCSs in midnight in S_Def 4 compared to S_Def 2 (Fig. 2h). When the requirement for area becomes stricter as can be seen from S_Def 5, the frequency of MCS decreases especially in July when the count increases by around 50 compared to S_Def 2 (Fig. 2g). Meanwhile, the afternoon MCS initiating during 2100–0600LST takes up more proportion while there are fewer afternoon MCSs (Fig. 2h).

The effects of varying thresholds on parameters including duration, speed, track length, and area exhibit semblance to those derived from radar reflectivity data. Increasing the duration threshold, as seen from the comparison between S_Def 3 and S_Def 2, yields an augmentation in the proportion of MCSs with fast speed, long life span, far track length, and large area. Striction of the area threshold (comparing S_Def 2 and S_Def 5) leads to an increased proportion of fast-moving and large-area MCSs, albeit contributing to a decrease in long-lived and far-traveling MCS percentage. A more lenient cloud top temperature threshold results in longer track length and life span, as well as faster propagation speed and larger area. However, the proportion of MCSs moving faster than 30km/h increases, which is a little different from the results derived from radar when the reflectivity threshold gets more lenient.

Figure 2 represents notable distinctions between MCS characteristics when using radar and satellite data, as they focus on different aspects of MCSs. For example, satellite-identified MCSs exhibit a diurnal cycle peak primarily in the afternoon, whereas radar-identified MCSs display a pronounced midnight peak. Overall, satellite-derived MCSs tend to have faster movement speeds, longer travel distances, and larger impact areas than those identified by radar. Disparities exist in the data and thresholds employed within the first group of definitions. For example, the minimum area requirements vary considerably in scale. Such discrepancies could result in the definitions within the first group identifying distinct systems or disparate segments of the same convective system, as compared to a complete system composed of stratiform and convection areas (defined by Satellite), where the area covered by the convection area (defined by Radar) is smaller. Radar reflectivity data primarily depicts precipitation by reflecting energy from precipitation targets. Figure S1 in the supporting information illustrates the precipitation exceeding 2mm/h (first column) and the radar reflectivity surpassing 35dBZ (second column) within the cloud shield of the MCS which was randomly selected, taking place on 26th June, 2015. Generally, the reflectivity pattern closely corresponds to the precipitation pattern, embedding within the large cold cloud shield area (orange shade) detected by Satellite. Despite the minimal influence of PFs (when set to 2mm/h) on MCS features, further investigation is needed to explore the impact of PF thresholds on MCSs characteristics. Therefore, the identification algorithm was improved by incorporating radar data as part of the PF determination to investigate PF threshold effects on MCS results. Next, we designed four threshold comparisons for the four aspects of PF, including radar reflectivity/precipitation amount, duration, and LWR, both for satellite-radar and satellite-IMERG, respectively (as shown in Figure 3).

Figs. 3a–f show that increasing the reflectivity threshold from 35 dBZ (S_R_Def 1) to 45 dBZ (S_R_Def 2) minimally affects MCS characteristics. However, a reduction in the duration threshold from 3 hours to 2 hours (S_R_Def 3) amplifies MCS counts, notably doubling in July compared to S_R_Def 1. Additionally, the diurnal cycle reflects an approximately 7% increase in afternoon-initiated MCSs (1500–1800LST). For the duration, a rise in MCSs with shorter lifespans accompanies a decrease in longer-lived MCSs proportion. Significantly, the proportion of MCSs with speeds in the 30–60 km/h range rises, while those exceeding 60 km/h decreases. Consequently, S_R_Def 3 reveals increasing MCSs with shorter travel distances (0–400 km) and fewer traveling exceeding 400 km. Regarding the area, the relaxation of the duration threshold primarily leads to a 6% increase in the proportion of MCSs within the 50,000–70,000 km^2 range, while the proportion of MCSs with exceptionally large area (≥150,000 km^2) decreases.

S_R_Def 4 compares the MCS characteristics without the LWR requirement. Notably, MCS counts surge considerably compared to S_R_Def 1, especially in July (Fig. 3a). From the diurnal cycle perspective, an approximately 8% increase in the afternoon-initiating MCSs percentage can be observed, while the midnight MCS proportion decreases (Fig. 3b). There is an increase in MCSs with a short lifespan of 3–7 hours, while fewer proportions of MCSs with a duration exceeding 7 hours (Fig. 3c). An increased proportion of MCSs with slow movement speeds of 0–30 km/h is noted, while those exceeding 30 km/h decreases (Fig. 3e). Track length demonstrates an approximately 20% increase in MCSs with short distance of 0–400 km and a decline in longer tracks exceeding 400 km (Fig. 3e). More MCSs have areas below 70,000 km^2 and fewer exhibit larger areas (Fig. 3f).

Figures 3g–l presents threshold comparisons for satellite-IMERG data. Comparing S_P_Def 1 and S_P_Def 2, increasing the precipitation intensity threshold from 2mm/h to 6mm/h insignificantly impacts MCS numbers in April, May, and September, but a noticeable reduction is observed during summer (JJA), as shown in Fig. 3g). Diurnally, S_P_Def 2 exhibits a higher proportion of early morning MCSs (0000–0900 LST) than S_P_Def 1, while the afternoon MCS proportion declines (Fig. 3h). S_P_Def 2 yields a slight 2% decrease in MCSs with a short lifespan of 3–7 hours, juxtaposed with an increase in those exceeding 7 hours compared to S_P_Def 1 (Fig. 3i). A decline in MCSs with slow speeds (0–30 km/h) coincides with an increase in those surpassing 60 km/h (Fig. 3k). This leads to a rise in the proportion of MCSs with longer track length (≥400km) (Fig. 3j). In terms of area, a decrease in the proportion of MCSs within the 30,000–50,000 km^2 range coincides with an increase in larger MCS areas exceeding 70,000 km^2 (Fig. 3l).

Raising the PF duration threshold from 2 to 3 hours (S_P_Def 3) has induced negligible alterations in MCS features. However, setting the LWR threshold for PF area to ≥2 (S_P_Def 4) triggers a notable MCS count reduction, particularly in July and August compared to S_P_Def 1 (Fig. 3g). Similar to S_P_Def 2, S_P_Def 4 experiences a decrease in afternoon MCSs and an increase in early morning MCSs. In terms of duration, S_P_Def 4 entails a decline of approximately 4% in MCSs with a short lifespan (3–7 hours), accompanied by an increase in those exceeding 7 hours (Fig. 3i). Regarding speed, a decrease in MCSs with slow movement speeds (≤60 km/h) aligns with an increase in faster-moving MCSs (Fig. 3k). Consequently, there is a rise in the proportion of MCSs covering longer travel distances (≥400 km) (Fig. 3j). In terms of area, there is an increase in the proportion of MCSs with larger areas (≥70,000km^2) (Fig. 3l).

Based on the statistical results, the utilization of radar reflectivity to detect PF (S_R_Def 1) tends to reduce the MCS counts in contrast to the adoption of IMERG precipitation data (S_P_Def 1). Furthermore, it increases (decrease) the proportion of MCSs occurring in the early morning (afternoon). This outcome may be attributed to the filtration effect introduced by the setting of 35 dBZ and the condition of LWR≥2. However, a noteworthy similarity is evident when the criterion LWR≥2 criterion is omitted (comparing S_R_Def 4 with S_P_Def 1). This result implies rationality in the selection of 35 dBZ thresholds, which corresponds to 2 mm/h precipitation in YHR. Referring to the study by Feng et al. (2021) and considering the restricted availability of radar data for further research progress, we choose to use S_P_Def 1 as the threshold for the subsequent analysis.

3.2 Spatial distribution of MCSs and related precipitation

Generally, 180 MCSs were detected from satellite Tb data from April to September during 2013–2018. The locations influenced by MCS, as well as the MCS precipitation amount and contribution to the total precipitation in AMJJAS, and then in three sub-seasons, are presented in Figure 4. The three sub-seasons, which are Pre-Meiyu within 1st May–14th June, Meiyu within 15th June–15th July, and Post-Meiyu within 16th

July–30th September, respectively, were selected based on the rainfall and environment of the Meiyu circulation over YHR (Ding, 1992; Mu et al. 2021). The region of Jiangsu Province downstream of the YHR exhibited the highest frequency of impacted locations, with about sixteen MCSs at each pixel annually (Fig. 4a). MCSs were least common in the Pre-Meiyu period among the three sub-seasons. The distribution center is south of Jiangsu Province, with roughly three MCSs (Fig. 4b). The number of MCSs rose during the Meiyu period. The center shifted northward by around 1 degree, with more than 6 MCSs occurring annually (Fig. 4c). During Post-Meiyu, the center continued to migrate northwardly and eventually reached 35°N (Fig. 4d). The extensive south-north range of MCSs during this period is likely due to the extended period (77 days) when the rainfall belt experienced northward and southward propagation.

The distribution of MCS precipitation shows consistency with the MCS frequency pattern and displays distinct seasonal characteristics. Throughout the AMJJAS, MCS precipitation is predominantly concentrated in the eastern part of Anhui Province, the southeastern part of Jiangsu Province, and the offshore eastern areas of Jiangsu (Fig. 4e). During the Pre-Meiyu season, MCS precipitation is mainly concentrated in the southern regions of Anhui and Jiangsu Provinces, averaging about 3mm/day (Fig. 4f). Transitioning into the Meiyu season, the MCS precipitation band shifts northward by 1–2 degrees and experiences a significant increase, peaking at over 6mm/day (Fig. 4g). In the Post-Meiyu season, MCS precipitation notably decreases, with the maximum reaching only 2.5mm/day (Fig. 4h).

The MCS precipitation contribution follows a similar pattern. During the warm season, the highest contribution of MCS precipitation on land reaches up to 20%, distributed across the eastern Anhui, southern Jiangsu, and southern Shandong Province (Fig. 4i). In the Pre-Meiyu season, the high contribution zone of MCS precipitation is situated around the boundary between Anhui and Jiangsu provinces, approximately at 32°N, reaching a maximum of 28% (Fig. 4j). During the Meiyu season, alongside the aforementioned high contribution area, another high contribution zone appears in the southern part of Shandong Province, reaching 32% (Fig. 4k). In the Post-Meiyu season, the relative contribution of MCS precipitation is the lowest, with the center retreating southward to approximately 31ºN in the southeastern corner of Jiangsu Province, with a maximum contribution of around 24% (Fig. 4l).

3.3 Characteristics of MCS and related precipitation

The probability density function (PDF) of the propagation direction of MCSs is presented in Figure 5a, and the propagation speed of the systems in 8 moving directions during the three sub-seasons is displayed in Figs. 5b–d. In this context, probability refers to the proportion of MCSs in a specific direction to the total number of MCSs. Eastward (E) propagating systems exhibit the highest proportion of MCSs, accounting for up to 45%, followed by northeast (NE) and southeast (SE) moving systems (Fig. 5a).

During the Pre-Meiyu season, eastward-moving MCS dominate, representing approximately 95% of all MCS during this period (Fig. 5b). In contrast, during the Meiyu (Fig. 5c) and Post-Meiyu (Fig. 5d) season, there is a higher proportion of MCSs exhibiting southward and westward movement compared to the Pre-Meiyu season. The windrose plots indicate that MCSs spread most rapidly during the Pre-Meiyu (Fig. 5b), with speeds within 60–90 km/h prevailing in the E and SE directions, accounting for up to 44% and 5%, respectively. Moreover, MCSs with speeds exceeding 90 km/h constitute about 35% of the total, a significantly higher proportion than in the other two sub-seasons. In the Meiyu season (Fig. 5c), MCSs exhibit the second-fastest movement speeds, and there is a higher proportion of MCS events with speeds above 60km/h compared to the Post-Meiyu season.

MCS features, including lifetime, track length, propagation speed, convective core area, cold cloud area, convective core precipitation mean rate, convective core precipitation area, cold cloud precipitation mean rate, and cold cloud precipitation area in three sub-seasons, are displayed in Figure 6. Meiyu MCSs had a relatively longer duration than other sub-seasons, with a medium duration of around 5 hours. The fastest MCS speed occurred during the Pre-Meiyu season, while the slowest is in the Post-Meiyu (Fig. 6c). Track length can thus be inferred from MCS propagation speed and lifetime characteristics (Fig. 6b). The Pre-Meiyu season stands out as the period when

MCSs typically propagated the farthest. 25% of MCSs traveled more than 1000 km, and the medium track length was approximately 400 km in this sub-season (Fig. 6b), primarily due to the rapid speed at that season (Fig. 6c). The convective core area of MCSs shows little noticeable difference across the three sub-seasons, except for MCSs in Meiyu season MCSs being slightly larger than those in the other two seasons (Fig. 6d). However, the cold cloud area varies significantly among the three sub-seasons, with the cold cloud areas the largest in Pre-Meiyu (Fig. 6e). The median area reaches 300,000 km^2, with 25% of the MCSs have an area of 450,000 km^2. Similarly, the convective core precipitation area exhibits its maximum extent in the Meiyu season, with the median and 75th percentile values being the highest among the three sub-seasons (Fig. 6f). In contrast, during the Pre-Meiyu season, the cold cloud precipitation was relatively smaller (Fig. 6f), even though the overall cold cloud precipitation area was the largest during this time (Fig. 6i). Whether considering the convective core or cold cloud precipitation mean rate (Figs. 6f, h), the Meiyu season consistently is the strongest, as evident from the highest median and 75th percentile values. Conversely, the Pre-Meiyu season experiences comparatively weaker average precipitation. This reflects that while cloud development within the cold cloud, apart from the convective core, is vigorous, the precipitation intensity remains significantly lower than during the Meiyu season.

Generally, MCSs may typically have the most significant impact on affected regions during the Meiyu season because of the most prolonged duration, largest convective core coverage area, and strongest precipitation intensity.

4. Large-scale circulation of MCSs

In this section, to comprehend the critical large-scale forcing mechanisms for MCSs in the YHR, we examine the large-scale environments associated with MCS initiation spanning the months of April to September (AMJJAS) and the three sub-seasons. The top-heavy diabatic heating profiles of MCSs, contributing to potential vorticity, have considerable influence on large-scale environments (Houze and Hobbs, 1982; Schumacher et al. 2013; Yang et al. 2017). To minimize the potential feedback of

MCSs on the large-scale environment, our analysis includes only the large-scale conditions at MCS initiation and the preceding three hours into the composites. Geopotential height (GH), specific humidity (Q), horizontal wind, and zonal wind (U) were analyzed. The anomalies depicted in each figure were calculated by subtracting the seasonal mean circulation from the circulation during MCS initiation within that specific season.

In both upper- and mid-level, MCS genesis within the southwest flow ahead of an upper-level trough (Figs. S3a, c), with higher specific humidity higher in YHR than the surroundings (Figs. S3b, d). The initiation region aligns with the northwest side of the subtropical high-GH system (500hPa, Fig. S3c and Fig. 8a). During the AMJJAS, the upper-level westerly jet axis is located around 40ºN, featuring a U wind speed of approximately 30m/s (Fig. 8a). YHR region experiences primarily easterly wind anomalies at the upper-level (200hPa, Fig. 8e), accompanied by upper-level divergence anomalies (200hPa, Fig. S5i) and lower-level divergence anomalies (925hPa, Fig. S5e). Coupled with mid-level upward motion (500hPa, Fig. S5a), these conditions foster convective growth and maintenance.

At the 700hPa level (Fig. 7a), the region of MCS initiation is positioned ahead of a low-GH system on the northwest side of the subtropical high-GH system over the ocean. Notably, this area is characterized by robust southwest winds exceeding 10m/s, facilitating the influx of warm and moist air. Anomaly fields unveil a prominent influence of a low-GH anomaly upon the YHR, accompanied by positive specific humidity anomalies approximating 3g/kg (Fig. 7e). Similar conditions prevailed at 850hPa, where strong southwesterly moist air flow into and through the YHR (Fig. S4). The anomaly flow pattern at 850hPa (Fig. S4e) exhibits southwesterly with maximum strength in the southeastern area of the initiation zone.

The large-scale environment for the three sub-seasons shows distinct differences. The influence of the subtropical high-GH system upon the YHR notably intensifies and shifts northward from the Pre-Meiyu season to the Post-Meiyu season, evident at 500hPa (Figs. 8a–d). Meanwhile, the upper-level westerly jet stream migrates northward, with peak MCS-mean zonal wind strongest during the Pre-Meiyu season, surpassing 40km/h. At 700hPa, both the Pre-Meiyu (Fig. 7b) and Meiyu (Fig. 7c) seasons experience southwest winds exceeding 10m/s, while such winds substantially decrease in the Post-Meiyu season (Fig. 7d). Furthermore, the Pre-Meiyu season witnesses the lowest average specific humidity (Fig. 7b), while in Meiyu season, the moisture is the most abundant. This phenomenon can be attributed to the enhanced capacity of warmer air to retain water vapor. Additionally, East Asian Monsoon plays an essential role, as the moisture transport is not well established until mid-June. During the Meiyu season, the moisture is transported from the Indian Ocean and the subtropical western Pacific, following a pathway along the southeastern coast of China established under the control of the East Asian Monsoon (Lim et al. 2002). Anomaly fields are the most pronounced in the Pre-Meiyu season (Fig. 7f). This sub-season exhibits the most notable low-GH anomaly within the YHR, reaching up to -10gpm. Q anomalies exceed 4g/kg, indicating a substantial moisture increase during MCSs initiate (Fig. 7f). Among the three sub-seasons, the Pre-Meiyu season displays the most prominent southwesterly wind anomaly, surpassing 5m/s (Fig. 7f). Conversely, while the Meiyu season has the highest average specific humidity, its specific humidity anomaly is the weakest, peaking at a modest 2g/kg (Fig. 7g). The GH anomaly is also weak. The YHR aligns between the centers of the low-GH anomaly and the high-GH anomaly, with the GH anomaly nearly negligible at the YHR center (Fig. 7g). The wind field anomaly is predominantly characterized by westerly wind components (Fig. 7g). During the Post-Meiyu season, the YHR experiences positive Q anomalies (approximately 3g/kg or lower) and low GH anomalies during MCS initiation (Fig. 7h). However, the gradient of the GH anomaly field is less pronounced than in the Pre-Meiyu season, yielding relatively weaker southwesterly wind anomalies (Fig. 7h). Moreover, during the Pre-Meiyu season, MCSs exhibit stronger lower-level convergence anomalies (Fig. S5f) and mid-level upward motion anomalies (Fig. S5b) at the time of their generation.

Upon examining the average field, it becomes evident that the Meiyu season displays higher average specific humidity and temperature at all levels, surpassing those observed during the Pre-Meiyu season. However, when Pre-Meiyu MCSs are forming, there are notable positive anomalies in upper-level GH (and negative anomalies in the lower level), as well as wet anomalies and southwestern jet stream anomalies, along with lower-level (upper-level) convergence (divergence) and mid-level upward motion, all of which are the most intense than in Meiyu season. This phenomenon could be attributed to the Meiyu front in the large-scale circulation during this sub-season providing a conducive environment for convection growth and resulting in relatively smaller anomalies. Furthermore, small-scale local perturbations may facilitate MCS growth in the absence of large-scale dynamical forcing when mean-state moisture is plentiful enough.

5. Summary and Discussion

This study used the high-resolution CPC-4km Tb dataset, radar observation, and IMERG precipitation dataset from 2013 to 2018 to examine the spatiotemporal characteristics and features of MCSs and related precipitation in the Yangtze-Huaihe River Basin (YHR) in eastern China from April to September and across three sub-seasons related to Meiyu season. The associated atmospheric large-scale environments of MCS initiation were also analyzed using the ERA5 reanalysis dataset. Furthermore, the impact of the selection of the dataset and threshold setting on the MCS features was investigated.

The choice of MCS definition significantly impacted the results of MCS features, including frequency, annual cycle, diurnal cycle, duration, propagation speed, track length, and coverage area (see Table S1) by comparing five different MCS thresholds using radar and satellite data. Fewer MCSs have been obtained for both radar and satellite data as the thresholds, including duration, radar reflectivity or Tb, area, duration, and LWR for radar, became stricter, and the morning-initiated MCS took up a larger proportion in the diurnal cycle. Comparisons between radar- and satellite-identified MCSs revealed distinctions. Satellite-identified MCSs exhibited afternoon diurnal peaks, faster movement speeds, longer travel distances, and expansive impact areas compared to radar-identified MCSs.

Further exploration of PF threshold impact on MCSs was conducted by incorporating radar with satellite as part of the PF determination. Stricter PF criteria intensified the morning peak of the MCS diurnal cycle and increased the proportion of faster-moving, long-track-length, larger and longer-lived MCSs. Additionally, the result implies rationality in the selection of 35 dBZ thresholds, which corresponds to 2 mm/h precipitation in YHR.

Generally, 180 MCSs were identified from satellite-IMERG data over the YHR during warm seasons from 2013 to 2018. The high-frequency centre of MCS distribution shifted northward from Pre-Meiyu to Post-Meiyu seasons. MCS precipitation shows consistency with MCS frequency. Eastward (E) propagating systems exhibit the highest proportion of MCSs, accounting for up to 45%, followed by northeast (NE) and southeast (SE) moving systems. 95% of Pre-Meiyu MCSs were eastward-moving, while a higher proportion exhibited southward and westward movement occurred in Meiyu and Post-Meiyu seasons compared to the Pre-Meiyu season. MCSs travel fastest during the Pre-Meiyu, followed by those in the Meiyu season.

The life duration of MCS in the Meiyu season was longer than other sub-seasons. Propagation speed was the slowest in the Post-Meiyu season and the fastest in the Pre-Meiyu season. Consequently, MCSs tended to travel the farthest during the Pre-Meiyu season. The convective core areas did not exhibit significant variation among the three sub-seasons except for the Meiyu season, when MCSs were slightly larger. Conversely, the cold cloud areas were the largest in the Pre-Meiyu season. During the Pre-Meiyu season, cold cloud precipitation was relatively smaller, even though the overall cold cloud precipitation area was the largest during this time. The area-average (for both convective cores and cold clouds) hourly MCS precipitation was the largest in the Meiyu season. Generally, MCSs typically had the most significant impact during the Meiyu season because of the most prolonged duration, largest convective core coverage area, and strongest precipitation intensity.

This study also investigated the large-scale atmospheric environments associated with MCS initiation over the YHR during the warm season. Generally, in the warm season, MCSs commonly initiated ahead of upper- and mid-level troughs and on the northwest side of the subtropical high-GH system. The YHR exhibited higher moisture levels compared to surrounding areas. A robust low-level southwest wind controlled the YHR, transporting warm and moist air. Strong low-level convergence and mid-level upward motion were observed over YHR. In the Pre-Meiyu season, the most significant anomalies were observed. During the Meiyu season, although moisture and temperature were more abundant and higher at all levels compared to the Pre-Meiyu season, the anomalies in the large-scale circulation were the weakest.

MCSs may exhibit different statistical characteristics depending on different chosen variables and threshold settings. Radars can capture MCS from the very beginning when convection cores start to form, while satellites observe MCSs by identifying their cold clouds. There are some possibilities that convective clouds dissipate before they are high or cold enough, which explains why fewer MCSs are derived by satellite than radar. Meanwhile, the high-altitude clouds associated with MCSs tend to propagate and immigrate faster than the ground-based convective cores, explaining the slightly longer duration, faster-and-farther propagation, and coverage area of satellite-derived MCSs. Threshold setting might also influence the detailed features of tracked MCSs. For example, the restriction of LWR strongly influences the diurnal cycle of MCSs. MCS characteristics differ significantly in various regions, so thresholds must be carefully selected accordingly.

Acknowledgments

The work is funded by the National Natural Science Foundation of China (U2242204, 41875124), and Jiangsu Education Department (KYCX22_0115). The authors also appreciate the NOAA's Climate Precipitation Center (CPC) for providing the infrared cloud top temperature data and ECMWF for supplying the hourly global reanalysis data ERA5. We declare no conflict of interest.

Data availability statement

CPC-4km half-hourly Brightness temperatures data (Janowiak et al. 2001), GPM IMERG v06 half-hourly precipitation data (Huffman et al. 2019), and the latest version of the hourly global reanalysis data ERA5 at pressure levels (ECMWF, 2017) are used in the creation of this manuscript.

All the data generated and the code (Lu et al. 2023) used in this study are open-sourced.

Table and Figure Captions

Table 1. Five definitions of MCSs using Satellite, Radar, and four definitions Satellite_IMERG and Satellite_Radar designed for threshold testing. Conv core represents convection core; PF represents precipitation feature; LWR represents length-width ratio.

Figure 1. (A) Topography over the Yangtze-Huaihe River Basin (YHR) and the distribution of 17 radar stations adopted in the YHR. The red circles represent the detection area of each station with a diameter of 230km. The black square denotes the analysis region in this study.

(a–l) Examples of 6 random-selected MCS cases identified utilizing the OT algorithm from radar (the first and third columns) and satellite (the second and fourth columns), respectively. (a, b) Case 1, 4th July 2013. (e, f) Case 2, 1st June 2014. (i, j) Case 3, 2nd June 2015. (c, d) Case 4, 2nd August. (g, h) Case 5, 10th June 2017. (k, l) Case 6, 18th August 2018. The contour represents the sum of MCS masks within their life span. The red contours are the boundaries of the areas affected by the MCSs. The blue dots denote the centroid of the system at each time slice, and the red lines connecting the blue dots represent the trajectories of each MCS. The gray rectangle indicates the analysis region of this study.

Figure 2. (1a) Annual cycle and (1b) diurnal cycle of MCS convection initiation, and PDFs of the (1c) duration, (1d) track length, total propagation distance of MCS centroid, (1e) speed, calculated as the division of track length by duration and (1f) convection core area, the average of convection core areas at each time step of MCSs derived from radar data using 5 definitions in the YHR.

(2a–2f) Same as (1a–1f) but for MCSs derived from satellite data using 5 definitions.

Figure 3. Same as Figure 2 but (1a–1f) for MCSs from satellite-radar data using 4 definitions, and (2a–2f) for MCSs derived from satellite-IMERG using 4 definitions.

Figure 4. Average spatial distributions of (a–d) MCS frequency, (e–h) MCS precipitation mean rate and (i–l) contribution fraction of MCS precipitation to the total precipitation in (a, e, i) AMJJAS, (b, f, j) Pre-meiyu, (c, g, k) Meiyu and (d, h, l) Post-meiyu during the period from 2013 to 2018.

Figure 5. (a) The frequency of MCSs moving in 8 directions. (b–g) Windrose plots of systems' propagation speed in (b) Pre-meiyu, (c) Meiyu and (d) Post-meiyu in 2013–2018.

Figure 6. Overall MCS features in three sub-seasons (Pre-meiyu, Meiyu and Post-meiyu) over the YHR: (a) MCS duration (unit: h); (b) MCS track length (unit: km); (c) MCS propagation speed (unit: km/h); (d) MCS convection core coverage area (unit: 10^4 km^2); (e) MCS cold cloud (CCS) coverage area (unit: 10^4 km^2), the average of cold cloud areas at each time step; (f) MCS convection core precipitation mean rate (unit: mm/h), the hourly average precipitation on each pixel within convection core of MCS; (g) MCS convection core precipitation area (unit: 10^4 km^2), the average of precipitation areas within convection core at each time step; (h) MCS CCS precipitation mean rate (unit: mm/h), the hourly average precipitation on each pixel within CCS of MCS; (i)

MCS cold cloud precipitation area (unit: 10^4 km^2), the average of precipitation areas within the cold clouds at each time step. The boxes indicate the interquartile range (25th and 75th percentiles), the horizontal bars inside the boxes denote the medium values and the whiskers represent 10th- and 90th- percentile values.

Figure 7. Composite (a, c) average and (b, d) anomaly of MCS initiation large-scale circulation at (a, b) 300hPa and (c, d) 500hPa levels in April–September during the period of 2013–2018. Shadings are specific humidity (unit: g/kg), arrows are wind (unit: m/s) and black contours are geopotential height (unit: gpm). The anomaly fields are calculated by subtracting the 6-year seasonal mean from the averaged field within three hours before the initiation of MCSs.

Figure 8. Same as in Figure 7, but for 200hPa zonal wind speed (shading, unit: m/s), 500hPa geopotential (contours, unit: gpm), and 200hPa wind (arrows, unit: m/s).

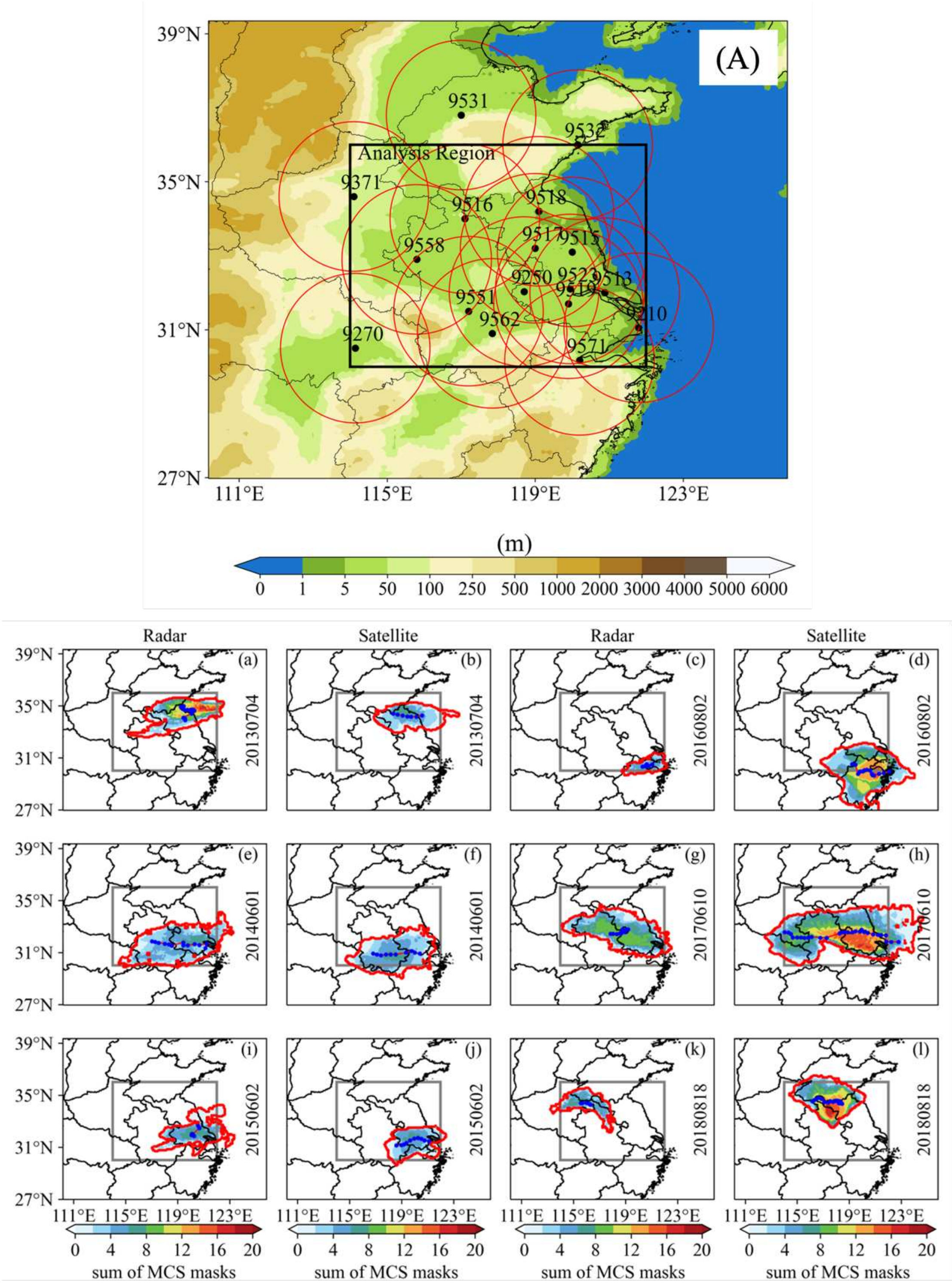

Figure 1. (A) Topography over the Yangtze-Huaihe River Basin (YHR) and the distribution of 17 radar stations adopted in the YHR. The red circles represent the detection area of each station with a diameter of 230km. The black square denotes the analysis region in this study.

(a–l) Examples of 6 random-selected MCS cases identified utilizing the OT algorithm from radar (the first and third columns) and satellite (the second and fourth columns), respectively. (a, b) Case 1, 4th July 2013. (e, f) Case 2, 1st June 2014. (i, j) Case 3, 2nd June 2015. (c, d) Case 4, 2nd August. (g, h) Case 5, 10th June 2017. (k, l) Case 6, 18th

August 2018. The contour represents the sum of MCS masks within their life span. The red contours are the boundaries of the areas affected by the MCSs. The blue dots denote the centroid of the system at each time slice, and the red lines connecting the blue dots represent the trajectories of each MCS. The gray rectangle indicates the analysis region of this study.

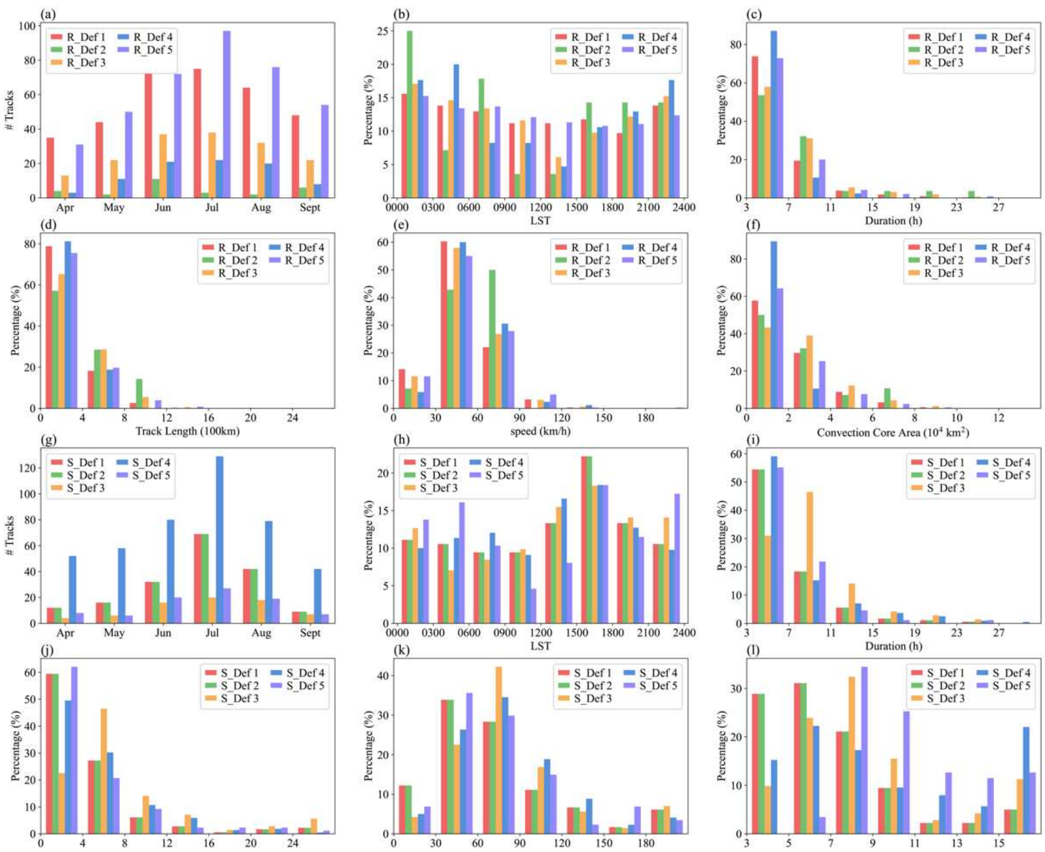

Figure 2. (a) Annual cycle and (b) diurnal cycle of MCS convection initiation, and PDFs of the (c) duration, (d) track length, total propagation distance of MCS centroid, (e) speed, calculated as the division of track length by duration and (f) convection core area, the average of convection core areas at each time step of MCSs derived from radar data using 5 definitions in the YHR.

(g–l) Same as (a–f) but for MCSs derived from satellite data using 5 definitions.

Figure 3. Same as Figure 2 but (a–f) for MCSs from satellite-radar data using 4 definitions, and (g–l) for MCSs derived from satellite-IMERG using 4 definitions.

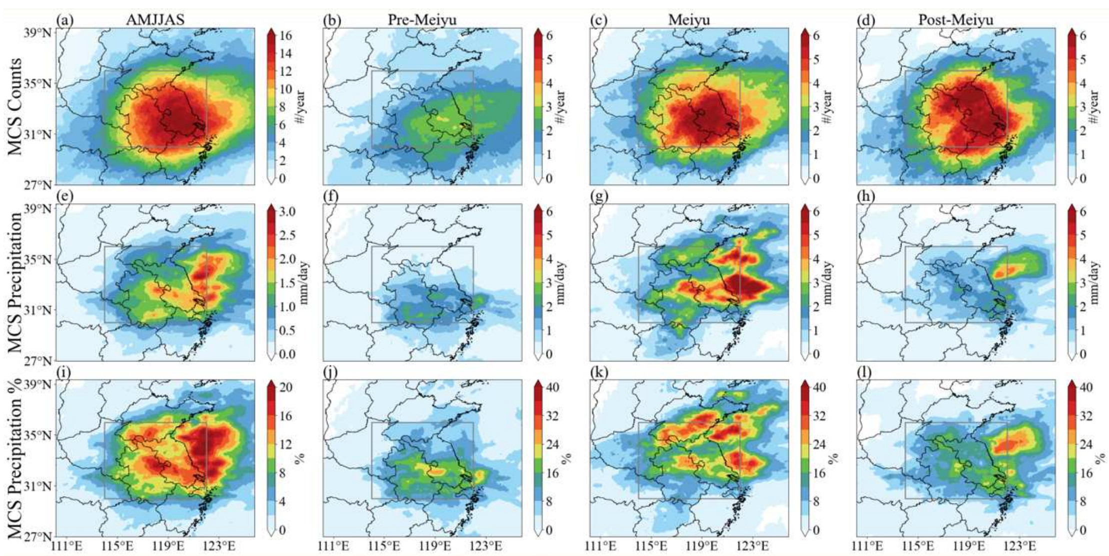

Figure 4. Average spatial distributions of (a–d) MCS frequency, (e–h) MCS precipitation mean rate and (i–l) contribution fraction of MCS precipitation to the total precipitation in (a, e, i) AMJJAS, (b, f, j) Pre-Meiyu, (c, g, k) Meiyu and (d, h, l) Post-Meiyu during the period from 2013 to 2018.

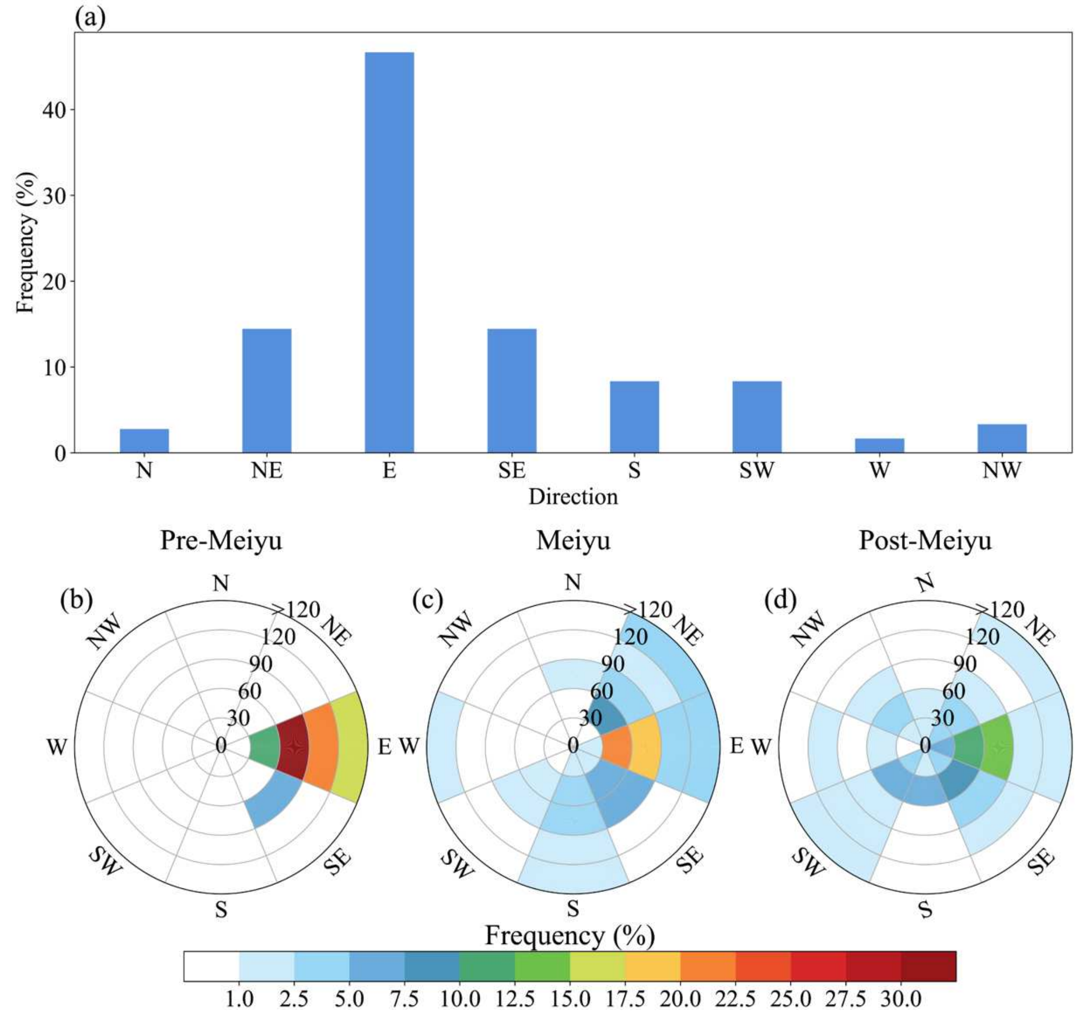

Figure 5. (a) The frequency of MCSs moving in 8 directions. (b–g) Windrose plots of systems' propagation speed in Pre-Meiyu (b), Meiyu (c) and Post-Meiyu (d) in 2013–2018.

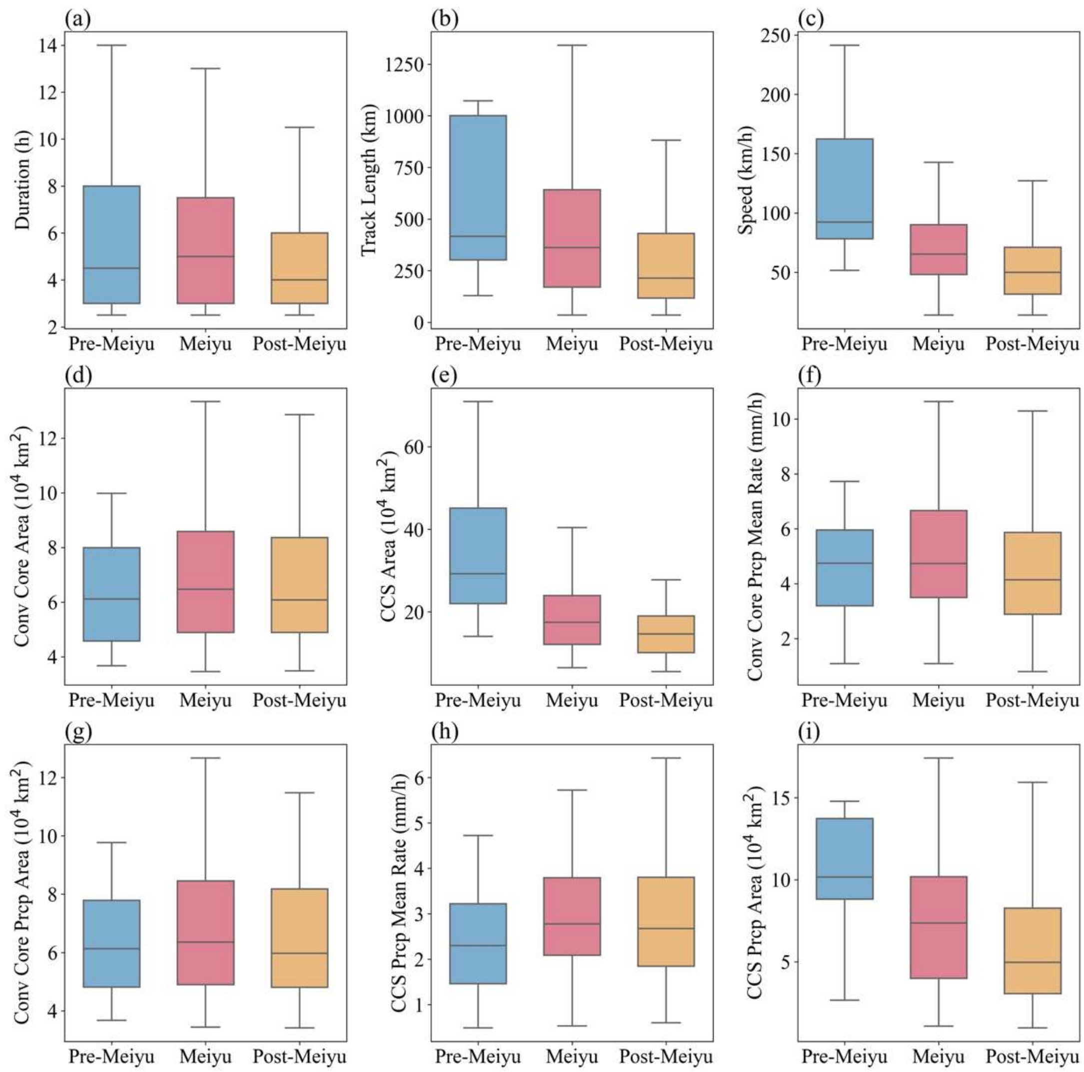

Figure 6. Overall MCS features in three sub-seasons (Pre-meiyu, Meiyu and Post-meiyu) over the YHR: (a) MCS duration (unit: h); (b) MCS track length (unit: km); (c) MCS propagation speed (unit: km/h); (d) MCS convection core coverage area (unit: 10^4 km^2); (e) MCS cold cloud (CCS) coverage area (unit: 10^4 km^2), the average of cold cloud areas at each time step; (f) MCS convection core precipitation mean rate (unit: mm/h), the hourly average precipitation on each pixel within convection core of MCS; (g) MCS convection core precipitation area (unit: 10^4 km^2), the average of precipitation areas within convection core at each time step; (h) MCS CCS precipitation mean rate (unit: mm/h), the hourly average precipitation on each pixel within CCS of MCS; (i) MCS cold cloud precipitation area (unit: 10^4 km^2), the average of precipitation areas within the cold clouds at each time step. The boxes indicate the interquartile range (25th and 75th percentiles), the horizontal bars inside the boxes denote the medium values and the whiskers represent 10th- and 90th- percentile values.

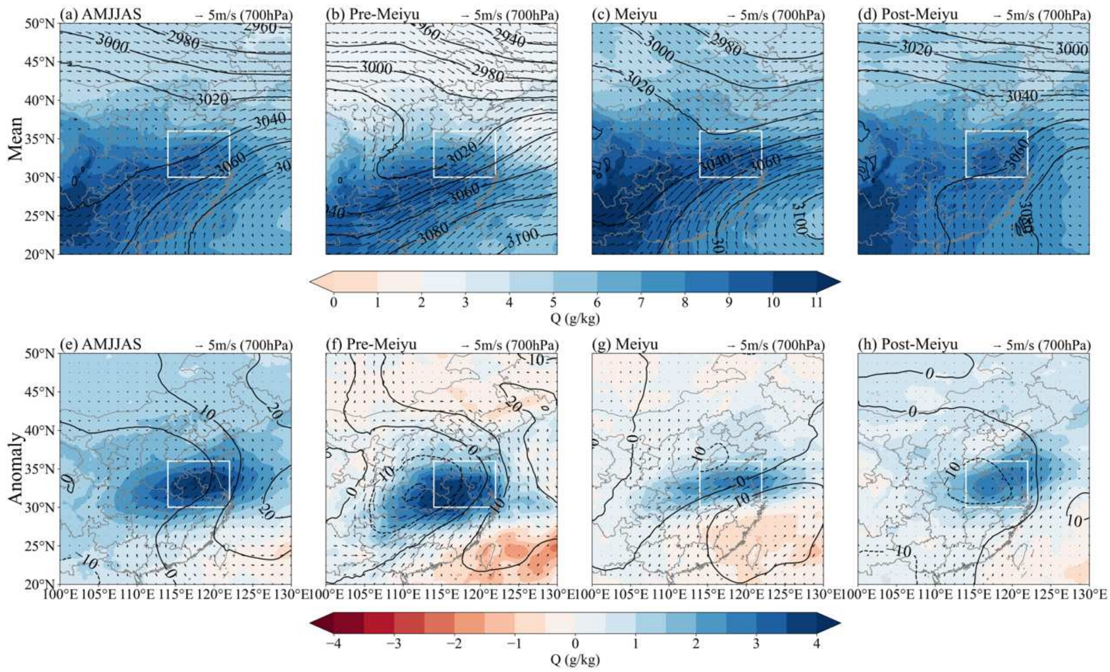

Figure 7. Composite (a–d) average and (e–h) anomaly of MCS initiation large-scale circulation at 700hPa level during MCS initiation in (a, e) April–September, (b, f) Pre-Meiyu, (c, g) Meiyu and (d, h) Post-Meiyu during the period of 2013–2018. Shadings are specific humidity (unit: g/kg), arrows are wind (unit: m/s) and black contours are geopotential height (unit: gpm).

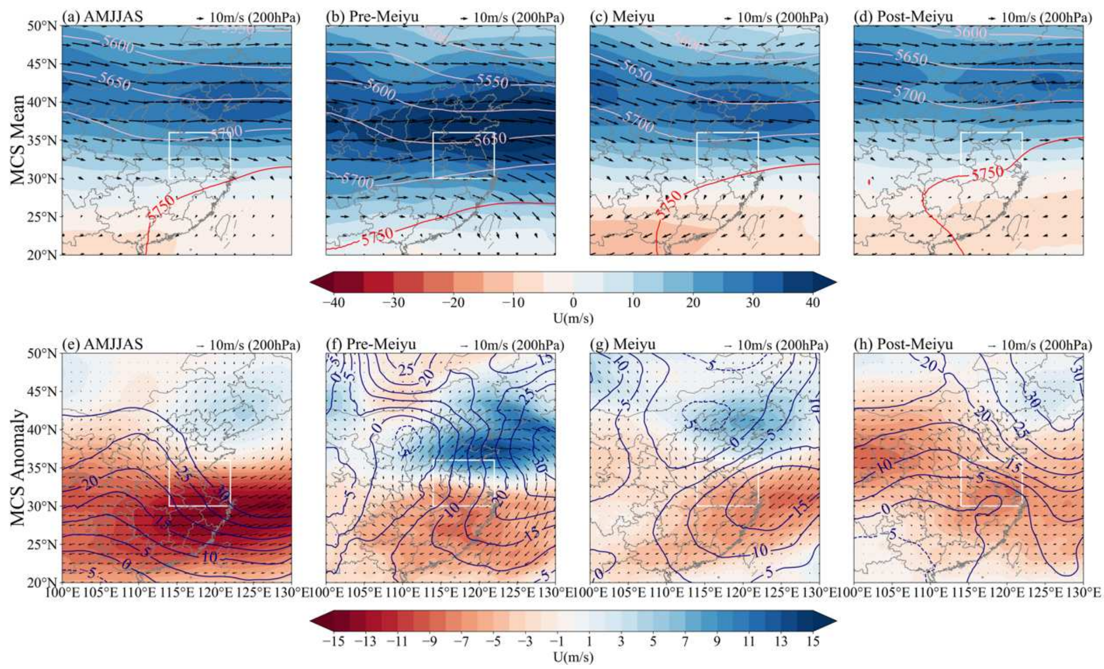

Figure 8. Same as in Figure 7, but for 200hPa zonal wind speed (shadings, unit: m/s), 500hPa geopotential (contours, unit: gpm), and 200hPa wind (arrows, unit: m/s).

Table 1. Five definitions of MCSs using Satellite, Radar, and four definitions Satellite_IMERG and Satellite_Radar designed for threshold testing. Conv core represents convection core; PF represents precipitation feature; LWR represents length-width ratio.

		Def1	Def2	Def3	Def4	Def5
Satellite	Conv core Tb (ºC)	⩽-52	⩽-52	⩽-52	⩽-38	⩽-52
	Conv core area (km^2)	⩾3,0000	⩾3,0000	⩾3,0000	⩾3,0000	⩾6,0000
	Cold cloud Tb (ºC)	⩽-32	⩽-32	⩽-23	⩽-23	⩽-32
	Cold cloud area (km^2)	⩾4,0000	⩾4,0000	⩾4,0000	⩾4,0000	⩾8,0000
	Duration (h)	⩾3	⩾3	⩾6	⩾3	⩾3
	PF rain rate (mm/h)	0	⩾2mm/h	⩾2mm/h	⩾2mm/h	⩾2mm/h
	PF duration (h)	0	⩾2	⩾2	⩾2	⩾2
	PF long axis (km)	0	⩾100	⩾100	⩾100	⩾100
Radar		Def1	Def2	Def3	Def4	Def5
	Conv core Reflectivity (dBZ)	⩾35	⩾35	⩾35	⩾40	⩾35
	Conv core area (km^2)	⩾1,000	⩾1,000	⩾1,000	⩾1,000	⩾2,000
	Cold cloud Reflectivity (dBZ)	⩾25	⩾25	⩾25	⩾25	⩾25
	Cold cloud area (km^2)	⩾2,000	⩾2,000	⩾2,000	⩾2,000	⩾3,200
	Duration (h)	⩾3	⩾3	⩾4	⩾3	⩾3
	LWR	2	4	2	2	2
	Long axis (km)	⩾100	⩾100	⩾100	⩾100	⩾100
Satellite_IMERG		S_P Def1	S_P Def2	S_P Def3	S_P Def4	
	Conv core Tb (ºC)	⩽-52	⩽-52	⩽-52	⩽-52	
	Conv core area (km^2)	⩾3,0000	⩾3,0000	⩾3,0000	⩾3,0000	
	Cold cloud Tb (ºC)	⩽-32	⩽-32	⩽-32	⩽-32	
	Cold cloud area (km^2)	⩾4,0000	⩾4,0000	⩾4,0000	⩾4,0000	
	Duration (h)	⩾3	⩾3	⩾3	⩾3	
	PF rain rate (mm/h)	⩾2	⩾6	⩾2	⩾2	
	PF duration (h)	⩾2	⩾2	⩾3	⩾2	
	PF LWR	0	0	0	⩾2	
	PF long axis (km)	⩾100	⩾100	⩾100	⩾100	
Satellite_Radar		S_R Def1	S_R Def2	S_R Def3	S_R Def4	
	Conv core Tb (ºC)	⩽-52	⩽-52	⩽-52	⩽-52	
	Conv core area (km^2)	⩾3,0000	⩾3,0000	⩾3,0000	⩾3,0000	
	Cold cloud Tb (ºC)	⩽-32	⩽-32	⩽-32	⩽-32	
	Cold cloud area (km^2)	⩾4,0000	⩾4,0000	⩾4,0000	⩾4,0000	
	Duration (h)	⩾3	⩾3	⩾3	⩾3	
	PF Reflectivity (dBZ)	⩾35	⩾45	⩾35	⩾35	
	PF duration (h)	⩾3	⩾3	⩾2	⩾3	
	PF LWR	2	2	2	0	
	PF long axis (km)	⩾100	⩾100	⩾100	⩾100	

References

Anselmo, E. M., Machado, L. A. T., Schumacher, C., & Kiladis, G. N. (2021). Amazonian mesoscale convective systems: Life cycle and propagation characteristics. International Journal of Climatology, 41(7), 3968–3981.

Atiah, W.A., Amekudzi, L.K., Danuor, S.K., 2023. Mesoscale convective systems and contributions to flood cases in Southern West Africa (SWA): A systematic review. Weather Clim. Extrem. 39, 100551. https://doi.org/10.1016/j.wace.2023.100551

Ayat, H., Evans, J. P., & Behrangi, A. (2021). How do different sensors impact IMERG precipitation estimates during hurricane days? Remote Sensing of Environment, 259, 112417.

Barnes, H. C., Zuluaga, M. D., & Houze Jr, R. A. (2015). Latent heating characteristics of the MJO computed from TRMM observations. Journal of Geophysical Research: Atmospheres, 120(4), 1322–1334.

Bartels, D. L., Skradski, J. M., & Menard, R. D. (1984). Mesoscale convective systems: A satellite-data-based climatology.

Bolvin, D. T., Huffman, G. J., Nelkin, E. J., & Tan, J. (2021). Comparison of Monthly IMERG Precipitation Estimates with PACRAIN Atoll Observations. Journal of Hydrometeorology, 22(7), 1745–1753.

Brewster, K., Hu, M., Xue, M., & Gao, J. (2005). Efficient assimilation of radar data at high resolution for short-range numerical weather prediction. In World Weather Research Program Symposium on Nowcasting and Very Short-Range Forecasting, WSN05, Tolouse, France, WMO, Symposium CD, Paper (Vol. 3).

Cetrone, J., & Houze Jr, R. A. (2009). Anvil clouds of tropical mesoscale convective systems in monsoon regions. Quarterly Journal of the Royal Meteorological Society: A Journal of the Atmospheric Sciences, Applied Meteorology and Physical Oceanography, 135(639), 305–317.

Chen, D., Guo, J., Yao, D., Lin, Y., Zhao, C., Min, M., et al. (2019). Mesoscale convective systems in the Asian monsoon region from Advanced Himawari Imager: Algorithms and preliminary results. Journal of Geophysical Research: Atmospheres, 124(4), 2210–2234.

Chen, X., Leung, L.R., Feng, Z., Yang, Q., 2022. Precipitation-Moisture Coupling Over Tropical Oceans: Sequential Roles of Shallow, Deep, and Mesoscale Convective Systems. Geophys. Res. Lett. 49, e2022GL097836. https://doi.org/10.1029/2022GL097836

Cheng, T. F., Dong, Q., Dai, L., & Lu, M. (2022). A dual regime of mesoscale convective systems in the East Asian Monsoon annual cycle. Journal of Geophysical Research: Atmospheres, 127(13), e2022JD036523.

Clark, A. J., Bullock, R. G., Jensen, T. L., Xue, M., & Kong, F. (2014). Application of object-based time-domain diagnostics for tracking precipitation systems in convection-allowing models. Weather and Forecasting, 29(3), 517–542.

Cui, W., Dong, X., Xi, B., Feng, Z., 2021. Climatology of Linear Mesoscale Convective

System Morphology in the United States based on Random Forests Method. J. Clim. 1–52. https://doi.org/10.1175/JCLI-D-20-0862.1

Ding, Y. (1992). Summer monsoon rainfalls in China. Journal of the Meteorological Society of Japan. Ser. II, 70(1B), 373–396.

European Centre for Medium-Range Weather Forecasts. (2017). ERA5 reanalysis (updated monthly) [Dataset]. Research Data Archive at the Climate Data Store (CDS) website. Retrieved from https://cds.climate.copernicus.eu/cdsapp#!/home

Feng, Z., Leung, L. R., Hagos, S., Houze, R. A., Burleyson, C. D., & Balaguru, K. (2016). More frequent intense and long-lived storms dominate the springtime trend in central US rainfall. Nature Communications, 7(1), 13429.

Feng, Z., Leung, L. R., Houze Jr, R. A., Hagos, S., Hardin, J., Yang, Q., et al. (2018). Structure and evolution of mesoscale convective systems: Sensitivity to cloud microphysics in convection-permitting simulations over the United States. Journal of Advances in Modeling Earth Systems, 10(7), 1470–1494.

Feng, Z., Houze, R. A., Leung, L. R., Song, F., Hardin, J. C., Wang, J., et al. (2019). Spatiotemporal characteristics and large-scale environments of mesoscale convective systems east of the Rocky Mountains. Journal of Climate, 32(21), 7303–7328.

Feng, Z., Leung, L. R., Liu, N., Wang, J., Houze Jr, R. A., Li, J., et al. (2021). A global high-resolution mesoscale convective system database using satellite-derived cloud tops, surface precipitation, and tracking. Journal of Geophysical Research: Atmospheres, 126(8), e2020JD034202.

Guo, Z., Tang, J., Tang, J., Wang, S., Yang, Y., Luo, W., & Fang, J. (2022). Object-based evaluation of precipitation systems in convection-permitting regional climate simulation over Eastern China. Journal of Geophysical Research: Atmospheres, 127(1), e2021JD035645.

Haberlie, A. M., & Ashley, W. S. (2019). A radar-based climatology of mesoscale convective systems in the United States. Journal of Climate, 32(5), 1591–1606.

Hayden, L., Liu, C., Liu, N., 2021. Properties of Mesoscale Convective Systems Throughout Their Lifetimes Using IMERG, GPM, WWLLN, and a Simplified Tracking Algorithm. J. Geophys. Res. Atmospheres 126, e2021JD035264. https://doi.org/10.1029/2021JD035264

Houze Jr, R. A., & Hobbs, P. v. (1982). Organization and structure of precipitating cloud systems. In Advances in Geophysics (Vol. 24, pp. 225–315). Elsevier.

Houze Jr, R. A., Rutledge, S. A., Biggerstaff, M. I., & Smull, B. F. (1989). Interpretation of Doppler weather radar displays of midlatitude mesoscale convective systems. Bulletin of the American Meteorological Society, 70(6), 608–619.

Houze Jr., R.A., 2004. Mesoscale convective systems. Rev. Geophys. 42. https://doi.org/10.1029/2004RG000150

Hu, H., Leung, L. R., & Feng, Z. (2020). Observed warm-season characteristics of MCS and non-MCS rainfall and their recent changes in the central United States. Geophysical Research Letters, 47(6), e2019GL086783.

Hu, H., Feng, Z., & Leung, L.-Y. R. (2021). Linking flood frequency with mesoscale convective systems in the US. Geophysical Research Letters, 48(9),

e2021GL092546.
Huffman, G.J., E.F. Stocker, D.T. Bolvin, E.J. Nelkin, Jackson Tan (2019), GPM IMERG Final Precipitation L3 Half Hourly 0.1 degree x 0.1 degree V06, Greenbelt, MD, Goddard Earth Sciences Data and Information Services Center (GES DISC), [Dataset], 10.5067/GPM/IMERG/3B-HH/06
Janowiak, J. E., Joyce, R. J., & Yarosh, Y. (2001). A real-time global half-hourly pixel-resolution infrared dataset and its applications. Bulletin of the American Meteorological Society, 82(2), 205–218. [Dataset] https://www.cpc.ncep.noaa.gov/products/global_precip/html/wpage.full_res.shtml
Jiang, L., & Bauer-Gottwein, P. (2019). How do GPM IMERG precipitation estimates perform as hydrological model forcing? Evaluation for 300 catchments across Mainland China. Journal of Hydrology, 572, 486–500.
Jirak, I. L., & Cotton, W. R. (2007). Observational analysis of the predictability of mesoscale convective systems. Weather and Forecasting, 22(4), 813–838.
Jirak, I. L., Cotton, W. R., & McAnelly, R. L. (2003). Satellite and radar survey of mesoscale convective system development. Monthly Weather Review, 131(10), 2428–2449.
Kukulies, J., Chen, D., & Curio, J. (2021). The role of mesoscale convective systems in precipitation in the Tibetan Plateau region. Journal of Geophysical Research: Atmospheres, 126(23), e2021JD035279.
Kukulies, J., Lai, H.-W., Curio, J., Feng, Z., Lin, C., Li, P., Ou, T., Sugimoto, S., Chen, D., 2023. Mesoscale convective systems in the third pole region: Characteristics, mechanisms and impact on precipitation. Front. Earth Sci. 11.
Li, P., Moseley, C., Prein, A. F., Chen, H., Li, J., Furtado, K., & Zhou, T. (2020). Mesoscale convective system precipitation characteristics over East Asia. Part I: Regional differences and seasonal variations. Journal of Climate, 33(21), 9271–9286.
Liu, Y., Yao, X., Fei, J., Yang, X., & Sun, J. (2021). Characteristics of mesoscale convective systems during the warm season over the Tibetan Plateau based on FY-2 satellite datasets. International Journal of Climatology, 41(4), 2301–2315.
Lu, Y., Tang, J., Xu, X., Tang, Y., & Fang, J. (2023). Characteristics of Warm-season Mesoscale Convective Systems over the Yangtze-Huaihe River Basin (YHR)—comparison between radar and satellite. [Dataset]. https://doi.org/10.5281/zenodo.8260134
Maddox, R. A. (1980). Mesoscale convective complexes. Bulletin of the American Meteorological Society, 1374–1387.
Moore, B.J., Neiman, P.J., Ralph, F.M., Barthold, F.E., 2012. Physical Processes Associated with Heavy Flooding Rainfall in Nashville, Tennessee, and Vicinity during 1–2 May 2010: The Role of an Atmospheric River and Mesoscale Convective Systems. Mon. Weather Rev. 140, 358–378. https://doi.org/10.1175/MWR-D-11-00126.1
Mu, X., Huang, A., Wu, Y., Xu, Q., Zheng, Y., Lin, H., Fang, D., Zhang, X., Tang, Y., Cai, S., 2021. Characteristics of the Precipitation Diurnal Variation and

Underlying Mechanisms Over Jiangsu, Eastern China, During Warm Season. Front. Earth Sci. 9. https://doi.org/10.3389/feart.2021.703071

Nesbitt, S. W., Cifelli, R., & Rutledge, S. A. (2006). Storm morphology and rainfall characteristics of TRMM precipitation features. Monthly Weather Review, 134(10), 2702–2721.

Pfister, L., Scott, S., Loewenstein, M., Bowen, S., & Legg, M. (1993). Mesoscale disturbances in the tropical stratosphere excited by convection: Observations and effects on the stratospheric momentum budget. Journal of Atmospheric Sciences, 50(8), 1058–1075.

Rehbein, A., Ambrizzi, T., & Mechoso, C. R. (2018). Mesoscale convective systems over the Amazon basin. Part I: climatological aspects. International Journal of Climatology, 38(1), 215–229.

Salio, P., Nicolini, M., & Zipser, E. J. (2007). Mesoscale convective systems over southeastern South America and their relationship with the South American low-level jet. Monthly Weather Review, 135(4), 1290–1309.

Schumacher, R. S., Clark, A. J., Xue, M., & Kong, F. (2013). Factors influencing the development and maintenance of nocturnal heavy-rain-producing convective systems in a storm-scale ensemble. Monthly Weather Review, 141(8), 2778–2801.

Tang, Y., Xu, X., Xue, M., Tang, J., & Wang, Y. (2020). Characteristics of low-level meso-γ-scale vortices in the warm season over East China. Atmospheric Research, 235, 104768.

Taylor, C. M., Belušić, D., Guichard, F., Parker, D. J., Vischel, T., Bock, O., et al. (2017). Frequency of extreme Sahelian storms tripled since 1982 in satellite observations. Nature, 544(7651), 475–478.

Wang, D., Giangrande, S. E., Schiro, K. A., Jensen, M. P., & Houze Jr, R. A. (2019). The characteristics of tropical and midlatitude mesoscale convective systems as revealed by radar wind profilers. Journal of Geophysical Research: Atmospheres, 124(8), 4601–4619.

Wang, J., Zhang, J. G., Wu, T., & others. (2019). MCS classification and characteristic analyses of extreme short-time severe rainfall in Hubei Province. Meteor Mon, 45(7), 931–944.

Wang, S. L., Kang, H. W., Gu, X. Q., & Ni, Y. Q. (2015). Numerical Simulation of Mesoscale Convective System in the Warm Sector of Beijing '7.21'Severe Rainstorm. Meteorol. Mon, 41, 544–553.

Wei, P., Xu, X., Xue, M., et al. (2023). On the Key Dynamical Processes Supporting the 21.7 Zhengzhou Record-breaking Hourly Rainfall in China. Advances in Atmospheric Sciences. 40(3): 337–349.

Xue, M., Droegemeier, K. K., & Wong, V. (2000). The Advanced Regional Prediction System (ARPS)–A multi-scale nonhydrostatic atmospheric simulation and prediction model. Part I: Model dynamics and verification. Meteorology and Atmospheric Physics, 75, 161–193.

Yang, Q., Houze Jr, R. A., Leung, L. R., & Feng, Z. (2017). Environments of long-lived mesoscale convective systems over the central United States in convection permitting climate simulations. Journal of Geophysical Research: Atmospheres,

122(24), 13–288.
Yang, X., Fei, J., Huang, X., Cheng, X., Carvalho, L. M. v, & He, H. (2015). Characteristics of mesoscale convective systems over China and its vicinity using geostationary satellite FY2. Journal of Climate, 28(12), 4890–4907.
Yin, J., Gu, H., Liang, X., Yu, M., Sun, J., Xie, Y., Li, F., Wu, C., 2022. A Possible Dynamic Mechanism for Rapid Production of the Extreme Hourly Rainfall in Zhengzhou City on 20 July 2021. J. Meteorol. Res. 36, 6–25. https://doi.org/10.1007/s13351-022-1166-7
Yun, Y., Liu, C., Luo, Y., & Gao, W. (2021). Warm-season mesoscale convective systems over eastern China: Convection-permitting climate model simulation and observation. Climate Dynamics, 57, 3599–3617.
Zheng, L., Sun, J., Zhang, X., & Liu, C. (2013). Organizational modes of mesoscale convective systems over central East China. Weather and Forecasting, 28(5), 1081–1098.